



Thermodynamic assessment and the composition prediction of amorphous alloy in the Fe–B–Er alloy system

S.L. Wang^{a,b}, J.J. Han^a, C.P. Wang^a, S.Z. Kou^c, X.J. Liu^{a,*}

^a Department of Materials Science and Engineering, College of Materials, and Research Center of Materials Design and Applications, Xiamen University, Xiamen 361005, PR China

^b College of Chemistry and Materials Science, Longyan University, Longyan 364000, Fujian, PR China

^c State Key Laboratory of Gansu Advanced Nonferrous Metal Materials, Lanzhou University of Technology, Lanzhou 730050, PR China

ARTICLE INFO

Article history:

Received 16 February 2011

Received in revised form 30 July 2011

Accepted 1 August 2011

Available online 16 September 2011

Keywords:

Phase diagrams

CALPHAD

Eutectic composition

Amorphous alloys

ABSTRACT

The phase diagrams and thermodynamic properties in the Fe–Er and B–Er binary systems have been assessed by using the CALPHAD (*Calculation of Phase Diagrams*) method on the basis of the experimental data including the thermodynamic properties and phase equilibria. The thermodynamic parameters of each phase in the Fe–Er and B–Er binary systems were obtained, and an agreement between the calculated results and experimental data was obtained in each binary system. The isothermal sections at different temperatures and liquidus surface in the Fe–B–Er system have been calculated based on the binary thermodynamic data assessed in the present work. In addition, by considering that the glass formation composition of amorphous alloy is closely relative to the eutectic point in corresponding phase diagram, the investigation of glass-forming ability (GFA) in Fe-rich alloys in the Fe–B–Er liquidus surface has also been implemented in this work. The experimental result indicates that the GFA of a certain alloy is intimately relative to its location in the phase diagram, which proves that the phase diagram is an efficient tool for the composition design of Fe-based amorphous alloy.

© 2011 Published by Elsevier B.V.

1. Introduction

Fe-based amorphous alloys have been paid much attention and have been widely used in electrical devices such as transformer cores due to its excellent magnetic properties, high endurance against cycled impact deformation and high corrosion resistance [1,2]. A great deal of effort has been devoted to predicting Fe-based amorphous alloys composition with good GFA [3–7], however, the effective guidance with regard to the composition design of Fe-based amorphous alloy has not been reported in multicomponent system. Thus, there is an urgent need to use a scientific approach to identify potential compositions of amorphous alloys in multicomponent system. Recently, the computational thermodynamic approach coupled with Turnbull's deep eutectic criterion [8] is considered to be a typically effective method to design the compositions of amorphous alloys [9–12]. However, it is difficult to exactly obtain the eutectic points in multicomponent system due to the lack of some binary or ternary thermodynamic data.

The addition of a small amount of rare-earth element, e.g. Ln (Ln is lanthanides) was found to be an effective method to improve the GFA of Fe-based BMG [5,6,13–15]. One of the most important functions of rare-earth element is to lower the liquidus temperature of

alloy. On the other hand, the significant change of potential precipitation by the addition of rare-earth element also plays a positive role in improving GFA [16]. Ternary Fe-based BMGs represented by the formulae $Fe_aM_bB_c$ are based on two simple selection rules [17]: (1) M is an element with atomic radius at least 130% that of Fe; (2) M possesses a eutectic point with Fe and the M–Fe eutectic is at the Fe-rich end. The M elements, Sc, Y, Dy, Ho and Er fulfill the two rules and exhibit BMG capability at the wide composition range. The purpose of this work is to investigate the relationship between the GFA of Fe–B–Er alloy and the Fe–B–Er ternary phase diagram. Recently, the Fe–Er system was thermodynamically assessed by Zhou et al. [18]. However, the magnetic contribution to the Gibbs energy in the phases bcc (Fe), fcc (Fe), $Fe_{17}Er_2$, $Fe_{23}Er_6$, Fe_3Er , and Fe_2Er was not considered. The Fe–Er system is reassessed in the present work. We firstly assessed the thermodynamic parameters for the phase diagrams in the Fe–Er and B–Er binary systems by means of the CALPHAD method, in which the thermodynamic parameters to describe the Gibbs free energy of the individual phases are optimized based on the experimental data of the thermodynamic properties and the phase diagram. Then, the isothermal sections at different temperatures and liquidus surface of the Fe–B–Er ternary system were calculated based on the binary thermodynamic data, and the Fe-rich alloys with the eutectic compositions were prepared by a single-roller melt-spinning technique to clarify the relationship between the GFA and phase diagram.

* Corresponding author. Tel.: +86 592 2187888; fax: +86 592 2187966.

E-mail address: lxj@xmu.edu.cn (X.J. Liu).

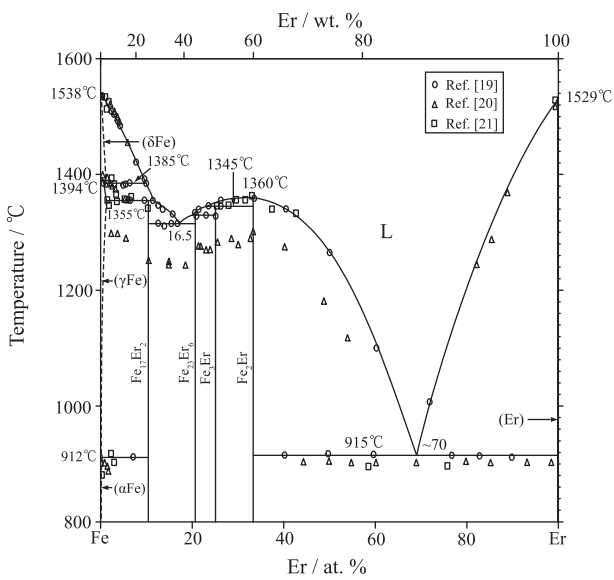


Fig. 1. The phase diagram of the Fe-Er system reviewed by Okamoto [22].

2. Experimental information

2.1. The Fe-Er system

The Fe-Er system consists of four solid solution phases (hcp (Er), αFe, γFe and δFe phases) and four intermetallic compounds (Fe₁₇Er₂, Fe₂₃Er₆, Fe₃Er, and Fe₂Er phases). Based on the differential thermal analysis, metallographic methods and X-ray powder diffraction, Buschow and Van der Goot [19] firstly investigated the phase diagram in the Fe-Er system and reported four intermetallic compounds (Fe₁₇Er₂, Fe₂₃Er₆, Fe₃Er, and Fe₂Er phases) and three peritectic reactions: L (10.5 at.% Er) + γFe ↔ Fe₁₇Er₂ at 1355 °C, L (19.1 at.% Er) + Fe₃Er ↔ Fe₂₃Er₆ at 1330 °C, and L (24 at.% Er) + Fe₂Er ↔ Fe₁₂Er at 1345 °C. Buschow and Van der Goot [19] also reported the melting point of Fe₂Er to be 1360 °C and determined two eutectic reactions: L (16.5 at.% Er) ↔ Fe₂₃Er₆ + Fe₁₂Er at 1315 °C, and L (~70 at.% Er) ↔ Fe₂Er + hcp (Er) at 915 °C. The eutectoid reaction of δFe ↔ γFe + L at 1385 °C was indicated in Ref. [19].

The phase diagram proposed by Meyer [20] was similar to that of Ref. [19] except that all the melting points of the compounds are lower than those of Ref. [19] by up to ~70 °C, however, Kolesnikov et al. [21] investigated the Fe-Er system and reported that all the melting points of the compounds are in agreement with the results of Ref. [19]. Based on the reported experimental data, Okamoto [22] compiled the Fe-Er phase diagram and indicated that the solubility of Er in bcc (Fe) and fcc (Fe) are less than 1 at.%. The phase diagram of the Fe-Er system reviewed by Okamoto [22] is shown in Fig. 1.

In addition, the mean values of the critical temperature for magnetic ordering and the Bohr magnetic moment of the Fe₁₇Er₂, Fe₂₃Er₆, Fe₃Er and Fe₂Er compounds were compiled by Buschow [23]. Norgren et al. [24] investigated the standard enthalpies of formation of the Fe₃Er and Fe₂Er phase by indirect solution calorimetry in liquid aluminum at 727 °C.

2.2. The B-Er system

The B-Er system consists of two solution phases (hcp (Er) and βB phases) and four intermetallic compounds (B₂Er, B₄Er, B₁₂Er and B₆₆Er phases). The phase diagram is based on the experimental data [25,26], and the liquidus curves were largely estimated by Spear [27]. The melting point of B₄Er phase reported to be 2360 °C [25] was accepted by Liao and Spear [28] over 2500 °C estimated by [26]. The phase diagram of the B-Er system reviewed by Liao and Spear [28] is shown in Fig. 2.

In addition, Meschel and Kleppa [29] measured the standard enthalpy of formation of the B₂Er phase by direct high-temperature reaction calorimetry at 1200 °C.

3. Thermodynamic models

Information about stable solid phases and the models used in the Fe-Er and B-Er binary systems is listed in Table 1.

3.1. Solution phases

In the Er-Fe and B-Er binary systems (which are both binary A-B systems), the Gibbs free energies of the liquid, fcc, bcc, hcp and

Table 1
The stable solid phases and the models used in the Fe-Er [39] and B-Er [28] systems.

System	Phase	Strukturbericht designation	Prototype	Modeling phase	Used models
Fe-Er	(αFe)	A2	W	BCC	SSM
	(γFe)	A1	CU	FCC	SSM
	(δFe)	A2	W	BCC	SSM
	Fe ₁₇ Er ₂	–	Ni ₁₇ Th ₂	(Fe) ₁₇ (Er) ₂	SM
	Fe ₂₃ Er ₆	–	Mn ₂₃ Th ₆	(Fe) ₂₃ (Er) ₆	SM
	Fe ₃ Er	–	–	(Fe) ₃ (Er)	SM
	Fe ₂ Er	–	Cu ₂ Mg	(Fe) ₂ (Er)	SM
	(Er)	A3	Mg	HCP	SSM
	(βB)	–	βB	Rhombohedral	SSM
	B ₂ Er	C32	AlB ₂	(B) ₂ (Er)	SM
B-Er	B ₄ Er	D1	ThB ₄	(B) ₄ (Er)	SM
	B ₁₂ Er	D2	UB ₁₂	(B) ₁₂ (Er)	SM
	B ₆₆ Er	–	ThB ₆₆	(B) ₆₆ (Er)	SM
	(Er)	A3	Mg	HCP	SSM

Note: SSM, substitutional solution model; SM, sublattice model.

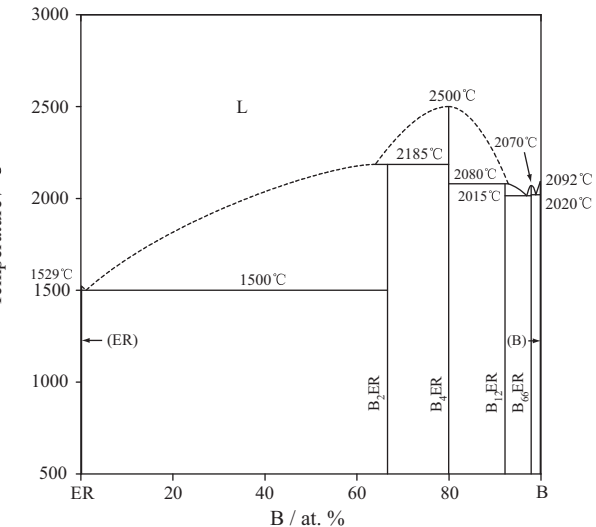


Fig. 2. The phase diagram of the B-Er system reviewed by Liao and Spear [28].

rhombohedral phases are described by the substitutional solution model, as follows:

$$G_m^\phi = \sum_{i=A,B}^0 G_i^\phi x_i + RT \sum_{i=A,B} x_i \ln x_i + \Delta^E G_m^\phi + \Delta^{mag} G_m^\phi, \quad (1)$$

where ${}^0 G_i^\phi$ is the Gibbs free energy of the pure component i in the respective reference state with the ϕ phase, which is taken from the SGTE pure element database [30]; x_i denotes the mole fraction of component i ; R is the gas constant; T is the absolute temperature; and the term $\Delta^E G_m^\phi$ represents the excess Gibbs free energy, which is expressed in Redlich-Kister polynomial form [31] as:

$$\Delta^E G_m^\phi = x_A x_B \sum_{m=0}^n L_{A,B}^\phi (x_A - x_B)^m, \quad (2)$$

$${}^i L_{A,B}^\phi = a + bT, \quad (3)$$

where ${}^i L_{A,B}^\phi$ is the binary interaction parameter, and the coefficients of a and b are constants to be evaluated on the basis of available experimental data.

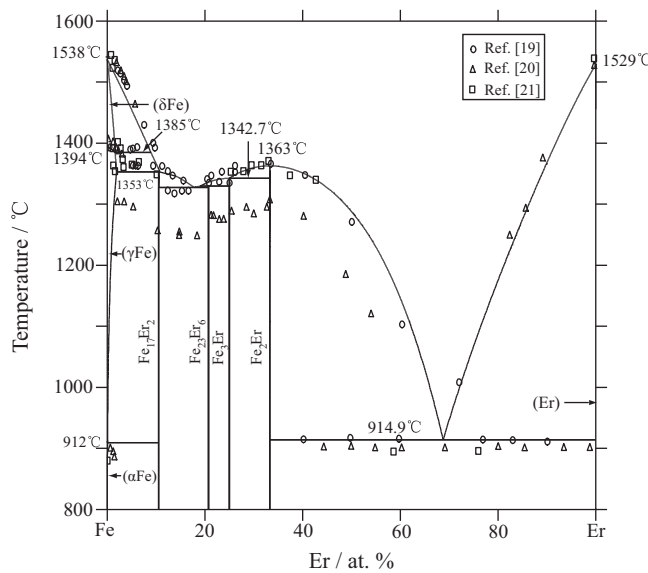
$\Delta^{mag} G_m^\phi$ is the magnetic contribution to the Gibbs free energy, which is described by the following equation [32]:

$$\Delta^{mag} G_m^\phi = RT \ln(\beta + 1)f(\tau) \quad (4)$$

Table 2

Experimental and calculated invariant reactions in the Fe–Er system.

Invariant reaction	Reaction type	Composition at.% Er			Temperature (°C)	Reference
$(\delta\text{Fe}) \leftrightarrow (\gamma\text{Fe}) + \text{L}$	Eutectoid	1.67	1.63	8.95	1385	[19]
$\text{L} + (\gamma\text{Fe}) \leftrightarrow \text{Fe}_{17}\text{Er}_2$	Peritectic	10.8	1.9	10.5	1355	[19]
$\text{L} \leftrightarrow \text{Fe}_{17}\text{Er}_2 + \text{Fe}_{23}\text{Er}_6$	Eutectic	16.5	10.5	10.5	1353	This work
$\text{L} + \text{Fe}_3\text{Er} \leftrightarrow \text{Fe}_{23}\text{Er}_6$	Peritectic	17.8	10.5	20.7	1327.5	[19]
$\text{L} + \text{Fe}_2\text{Er} \leftrightarrow \text{Fe}_3\text{Er}$	Peritectic	19.0	25	20.7	1330	This work
$\text{L} \leftrightarrow \text{Fe}_2\text{Er}$	Congruent	25.0	33.3	25	1345	[19]
$\text{L} \leftrightarrow \text{Fe}_2\text{Er} + (\text{Er})$	Eutectic	~70	33.3	33.3	1342.7	This work
		68.7	33.3	33.3	1360	[19]
			100	100	915	This work
			33.3	33.3	914.9	[19]
						This work

**Fig. 3.** Calculated phase diagram of the Fe–Er system compared with the experimental data [19–21].

where $\tau = T/T_C^\phi$, T_C^ϕ is the Curie temperature of solution for ferromagnetic ordering and β is the Bohr magneton number, the function $f(\tau)$ is formulated by the polynomial of the normalized temperature, as follows:

$$f(\tau) = 1 - \frac{[(79\tau^{-1}/140p) + (474/497)((1/p) - 1)((\tau^3/6) + (\tau^9/135) + (\tau^{15}/600))]}{D} \quad \text{for } \tau \leq 1 \quad (5)$$

$$f(\tau) = \frac{(\tau^{-5}/10) + (\tau^{-15}/315) + (\tau^{-25}/1500)}{D} \quad \text{for } \tau > 1 \quad (6)$$

$$D = \frac{518}{1125} + \frac{11,692}{15,975} \left(\frac{1}{p} - 1 \right) \quad (7)$$

where p depends on the structure, 0.40 for bcc structure and 0.28 for others.

Since the fcc and bcc phase in Fe–Er system are magnetic phases, thus the magnetic contribution ($\Delta^{\text{mag}}G_m^{\text{fcc}}$ and $\Delta^{\text{mag}}G_m^{\text{bcc}}$) to the Gibbs free energy in these phases was considered in the present work.

3.2. Stoichiometric intermetallic compounds

The intermetallic compounds of the $\text{Fe}_{17}\text{Er}_2$, $\text{Fe}_{23}\text{Er}_6$, Fe_3Er , Fe_2Er , B_2Er , B_4Er , B_{12}Er and B_{66}Er phases in the Fe–Er and B–Er binary systems are all treated as stoichiometric phases, because no reliable experimental data about the homogeneity range of these

compounds are available. The Gibbs free energy per mole of formula unit $M_p\text{Er}_q$ can be expressed as follows:

$$G_{M:\text{Er}}^{\text{M}_p\text{Er}_q} = p^0 G_M^{\text{SER}} + q^0 G_{\text{Er}}^{\text{SER}} + \Delta^0 G_f^{\text{M}_p\text{Er}_q} + \Delta^{\text{mag}} G_m^{\text{M}_p\text{Er}_q}, \quad (8)$$

where $\Delta^0 G_f^{\text{M}_p\text{Er}_q}$ indicates the standard Gibbs free energy of formation of the stoichiometric compound from pure elements, which is described as:

$$\Delta^0 G_f^{\text{M}_p\text{Er}_q} = a' + b'T, \quad (9)$$

where the parameters a' and b' are evaluated in the present work.

$\Delta^{\text{mag}} G_m^{\text{M}_p\text{Er}_q}$ is magnetic contribution to the Gibbs free energy, which is expressed in Eqs. (4)–(7), where β and T_C^ϕ of each intermetallic compound are taken from the literature [23].

Since the $\text{Fe}_{17}\text{Er}_2$, $\text{Fe}_{23}\text{Er}_6$, Fe_3Er and Fe_2Er intermetallic compounds are magnetic phases, thus the magnetic contribution ($\Delta^{\text{mag}} G_m^{\text{Fe}_p\text{Er}_q}$) to the Gibbs free energy in these phases was considered in the present work.

4. Optimized results and discussion

The optimization of the thermodynamic parameters was carried out by using the PARROT program in the Thermo-Calc software [33], which can handle various kinds of experimental data. The experimental data of the phase diagram and thermodynamic properties were used as input to the program. Each piece of selected information was given a certain weight based on the importance of the data,

and changed by trial and error during the assessment, until most of the selected experimental information was reproduced within the expected uncertainty limits.

4.1. The Fe–Er system

The calculated Fe–Er phase diagram compared with the experimental data is shown in Fig. 3, and the calculated compositions and temperatures for the invariant reactions compared with the selected experimental data are listed in Table 2. It is seen that the calculated results are in reasonable agreement with the experimental data [19–21], except for the temperature of eutectic reaction ($\text{L} \leftrightarrow \text{Fe}_{23}\text{Er}_6 + \text{Fe}_{17}\text{Er}_2$), which shows a discrepancy of 12 °C between the calculated results and the experimental data. A set of complete self-consistent thermodynamic parameters describing the Gibbs free energy of each phase in the Fe–Er system is given in Table 3.

Table 3

Thermodynamic parameters in the Fe–Er system assessed in the present work.

Parameters in each phase (J/mol)

Liquid phase, format (Fe, Er)

$$\Omega_{\text{Fe},\text{Fr}}^{\text{Liq}} = 55,725 + 26.972T$$

$$\Omega_{\text{Fe},\text{Fr}}^{\text{Liq}} = -6594 + 0.672T$$

$$\Omega_{\text{Fe},\text{Fr}}^{\text{Liq}} = 9756 - 8.014T$$

Bcc phase, format (Fe, Er)

$$\Omega_{\text{Fe},\text{Fr}}^{\text{Bcc}} = 17,130$$

Fcc phase, format (Fe, Er)

$$\Omega_{\text{Fe},\text{Fr}}^{\text{Fcc}} = 13,250$$

Hcp phase, format (Fe, Er)

$$\Omega_{\text{Fe},\text{Fr}}^{\text{Hcp}} = 40,000$$

Fe_2Er phase, format $(\text{Fe})_{0.667}(\text{Er})_{0.333}$

$$\Delta^0 G_{\text{Fe}_2\text{Er}}^f = -18,180 + 5.311T$$

$$T_{\text{C}}^{\text{Fe}_2\text{Er}} = 587, \text{ Ref. [23]}$$

$$\beta^{\text{Fe}_2\text{Er}} = 4.85, \text{ Ref. [23]}$$

Fe_3Er phase, format $(\text{Fe})_{0.75}(\text{Er})_{0.25}$

$$\Delta^0 G_{\text{Fe}_3\text{Er}}^f = -15,460 + 4.655T$$

$$T_{\text{C}}^{\text{Fe}_3\text{Er}} = 552, \text{ Ref. [23]}$$

$$\beta^{\text{Fe}_3\text{Er}} = 3.45, \text{ Ref. [23]}$$

$\text{Fe}_{17}\text{Er}_2$ phase, format $(\text{Fe})_{0.895}(\text{Er})_{0.105}$

$$\Delta^0 G_{\text{Fe}_{17}\text{Er}_2}^f = -10,581 + 3.985T$$

$$T_{\text{C}}^{\text{Fe}_{17}\text{Er}_2} = 305, \text{ Ref. [23]}$$

$$\beta^{\text{Fe}_{17}\text{Er}_2} = 17.1, \text{ Ref. [23]}$$

$\text{Fe}_{23}\text{Er}_6$ phase, format $(\text{Fe})_{0.793}(\text{Er})_{0.207}$

$$\Delta^0 G_{\text{Fe}_{23}\text{Er}_6}^f = -14,010 + 4.431T$$

$$T_{\text{C}}^{\text{Fe}_{23}\text{Er}_6} = 480, \text{ Ref. [23]}$$

$$\beta^{\text{Fe}_{23}\text{Er}_6} = 32, \text{ Ref. [23]}$$

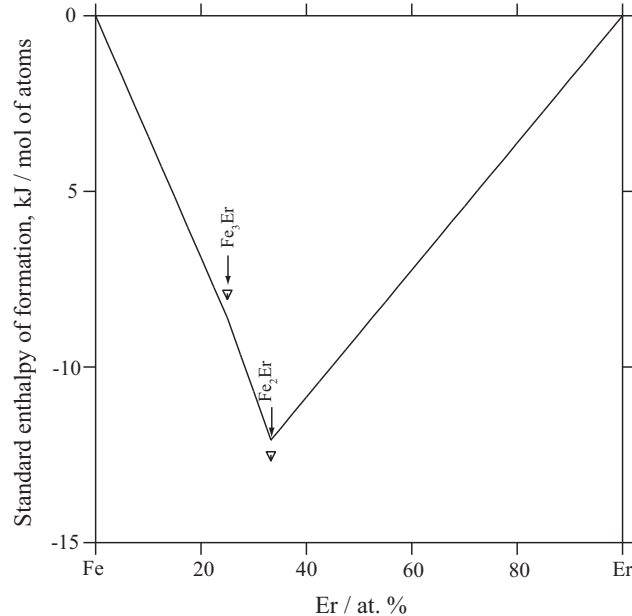


Fig. 4. Calculated standard enthalpies of formation at 25 °C with reference states of αFe (bcc) and Er (hcp) in the Fe–Er system compared with the experimental data [24].

The calculated standard enthalpies of formation at 25 °C with reference states of the αFe (bcc) and Er (hcp) phases compared with the experimental data [23] are presented in Fig. 4. It is seen that an agreement is obtained between the calculated results and the experimental data.

4.2. The B–Er system

The calculated B–Er phase diagram compared with the experimental data is shown in Fig. 5, and the calculated compositions and temperatures for the invariant reactions compared with the selected experimental data are listed in Table 4. It is seen that the

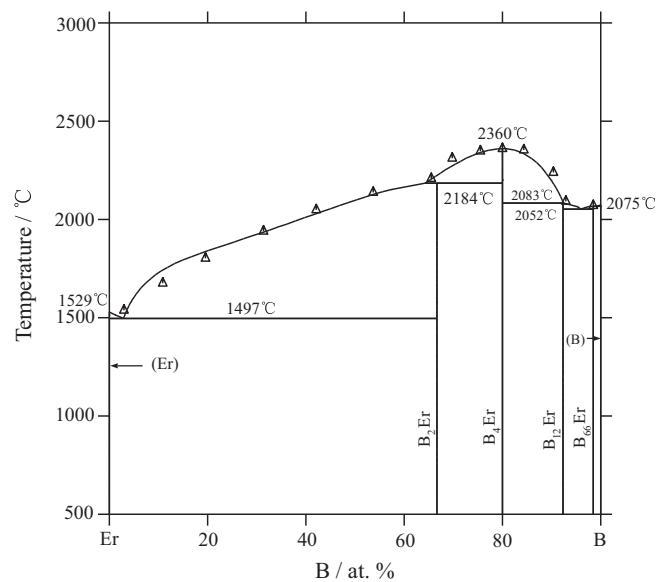


Fig. 5. Calculated phase diagram of the B–Er system compared with the experimental data [28].

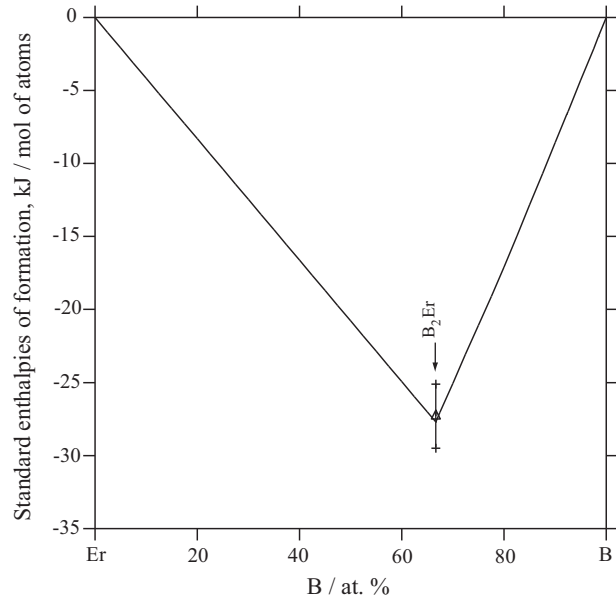


Fig. 6. Calculated standard enthalpies of formation at 25 °C with reference states of βB (rhombohedral) and Er (hcp) in the B–Er system compared with the experimental data [29].

calculated results are in reasonable agreement with the experimental data [28]. A set of complete self-consistent thermodynamic parameters describing the Gibbs free energy of each phase in the B–Er system is given in Table 5.

In addition, the eutectic reactions ($\text{L} \leftrightarrow \text{B}_{66}\text{Er} + \beta\text{B}$ and $\text{L} \leftrightarrow \text{B}_{12}\text{Er} + \text{B}_{66}\text{Er}$) in Liao's work [28] cannot be reproduced by using the present parameters, because the liquidus slope around the B_{66}Er phase is too steep, which is thermodynamically unlikely [34]. Based on the present parameters, the calculated temperatures of the eutectic reactions ($\text{L} \leftrightarrow \text{B}_{66}\text{Er} + \beta\text{B}$ and $\text{L} \leftrightarrow \text{B}_{12}\text{Er} + \text{B}_{66}\text{Er}$) are above the experimental data [28], which is more acceptable. These calculated results need to be determined by experiments in the future.

The calculated standard enthalpies of formation at 25 °C with reference states of the βB (rhombohedral) and Er (hcp) phases are

Table 4
Special points of the B–Er system.

Invariant reaction	Reaction type	Composition at.% B			Temperature (°C)	Reference
$L \leftrightarrow (Er) + B_2Er$	Eutectic	~1.0	0	66.7	1500	[28]
		2.9	0	66.7	1497	This work
$L + B_4Er \leftrightarrow B_2Er$	Peritectic	65	80	66.7	2185	[28]
		64.3	80	66.7	2184	This work
$L \leftrightarrow B_4Er$	Congruent		80		2360	[28]
			80		2360	This work
$L + B_4Er \leftrightarrow B_{12}Er$	Peritectic	93.0	80	92.3	2083	[28]
		92.5	80	92.3	2083	This work
$L \leftrightarrow B_{12}Er + B_{66}Er$	Eutectic	~97	92.3	98.5	2015	[28]
		96.0	92.3	98.5	2052	This work
$L \leftrightarrow B_{66}Er$	Congruent		98.5		2070	[28]
			98.5		2070	This work
$L \leftrightarrow B_{66}Er + \beta B$	Eutectic	~99	98.5	100	2020	[28]
		99.2	98.5	100	2067	This work

Table 5
Thermodynamic parameters in the B–Er system assessed in the present work.

Parameters in each phase (J/mol)	
Liquid phase, format (B, Er)	
${}_0L_{B,Er}^{Liq}$	= -80, 742 + 24.399T
${}_1L_{B,Er}^{Liq}$	= -60, 000 + 6.6T
${}_2L_{B,Er}^{Liq}$	= 16, 500 – 15.0T
${}_3L_{B,Er}^{Liq}$	= -3.0T
Hcp phase, format (B, Er)	
${}_0L_{B,Er}^{Hcp}$	= 50, 000
B_2Er phase, format (B) _{0.667} (Er) _{0.333}	
$\Delta^0G_{B:Er}^{B_2Er}$	= -27, 700 + 1.0T
B_4Er phase, format (B) _{0.8} (Er) _{0.2}	
$\Delta^0G_{B:Er}^{B_4Er}$	= -17, 100 – 3.31T
$B_{12}Er$ phase, format (B) _{0.9231} (Er) _{0.0769}	
$\Delta^0G_{B:Er}^{B_{12}Er}$	= -6600 – 2.075T
$B_{66}Er$ phase, format (B) _{0.985} (Er) _{0.015}	
$\Delta^0G_{B:Er}^{B_{66}Er}$	= -1300 – 0.655T

Table 6
The adopted thermodynamic parameters in the Fe–B [35] system in the present work.

Parameters in each phase (J/mol)	
Liquid phase, format (Fe, B)	
${}_0L_{Fe,B}^{Liq}$	= -133, 438 + 33.95T
${}_1L_{Fe,B}^{Liq}$	= 7771
${}_2L_{Fe,B}^{Liq}$	= 29, 739
Bcc phase, format (Fe, B)	
${}_0L_{Fe,B}^{Bcc}$	= -47, 920 + 42.09T
Fcc phase, format (Fe, B)	
${}_0L_{Fe,B}^{Fcc}$	= -58, 211 + 49.9T
Fe_2B phase, format (Fe) _{0.667} (B) _{0.333}	
$\Delta^0G_{f}^{Fe_2B}$	= -26, 261 + 3.466T
FeB phase, format (Fe) _{0.5} (B) _{0.5}	
$\Delta^0G_f^{FeB}$	= -35, 287 + 5.922T

presented in Fig. 6 with the experimental data [29]. It is seen that the calculated enthalpy of formation of the B_2Er phase is in agreement with the experimental data.

4.3. The Fe–B–Er system extended from binary systems

The phase equilibria in the Fe–B–Er ternary system are useful for the development of new materials. However, no information about the phase equilibria and thermodynamic properties in the Fe–B–Er ternary system has been reported. In this work, the isothermal sections at different temperatures and liquidus surface of the Fe–B–Er system were calculated based on the binary thermodynamic parameters of the Fe–B [35], Fe–Er and B–Er binary systems. The adopted thermodynamic parameters of the Fe–B [35] system are listed in Table 6. Fig. 7 shows the calculated phase

Table 7
The calculated eutectic reactions of the Fe–B–Er system in the Fe-rich region.

No.	Reaction type	Reaction temperature (°C)	Composition (at.%)		
			Fe	B	Er
E ₁	$L \leftrightarrow Fe_2B + Fe_{17}Er_2 + \gamma Fe$	1125.9	80.9	15.2	3.9
E ₂	$L \leftrightarrow Fe_2B + Fe_3Er + Fe_{23}Er_6$	1107.9	72.6	15.9	11.5
E ₃	$L \leftrightarrow Fe_2Er + Fe_2B + Fe_3Er$	1108.0	69.2	16.7	14.1

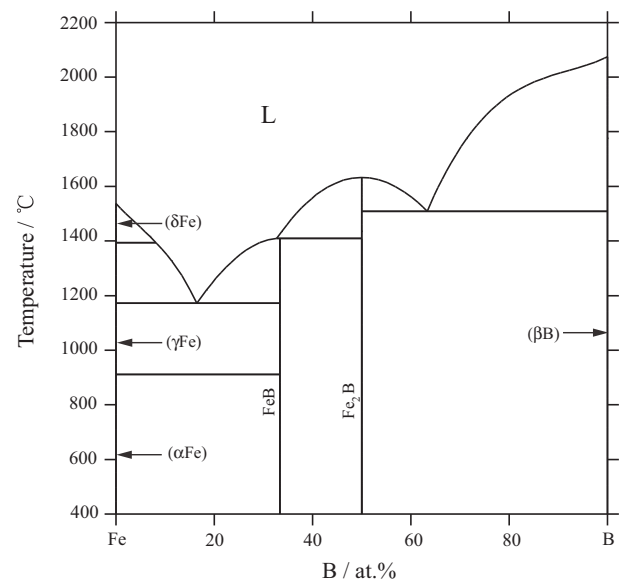


Fig. 7. The calculated phase diagram of the Fe–B system [35].

diagram of the Fe–B system [35]. The calculated isothermal sections at 500, 900, and 1200 °C are shown in Fig. 8. From Fig. 8a and b, it is found that four three-phase regions of the $Liq + Fe_2Er + Fe_3Er$, $Liq + Fe_{23}Er_6 + Fe_3Er$, $Liq + Fe_{23}Er_6 + Fe_{17}Er_2$, $Liq + Fe_{17}Er_2 + FCC$ and five two-phase regions of the $Liq + Fe_3Er$, $Liq + Fe_{23}Er_6$, $Liq + Fe_{17}Er_2$, $Liq + Fe_2B$, $Liq + FCC$ change to another four three-phase regions of the $Fe_2B + Fe_2Er + Fe_3Er$, $Fe_2B + Fe_3Er + Fe_{23}Er_6$, $Fe_2B + Fe_{17}Er_2 + Fe_{23}Er_6$, $Fe_2B + Fe_{17}Er_2 + BCC$ in Fe-rich region. With the decreasing of temperature, these phase regions remain unchanged as shown in Fig. 8c. The calculated liquidus surface of the Fe–B–Er system is shown in Fig. 9, where there are three eutectic reactions in the Fe-rich region, as given in Table 7. Although the liquidus surface in ternary system is obtained by extrapolating from binary thermodynamic parameters, this predicted liquidus

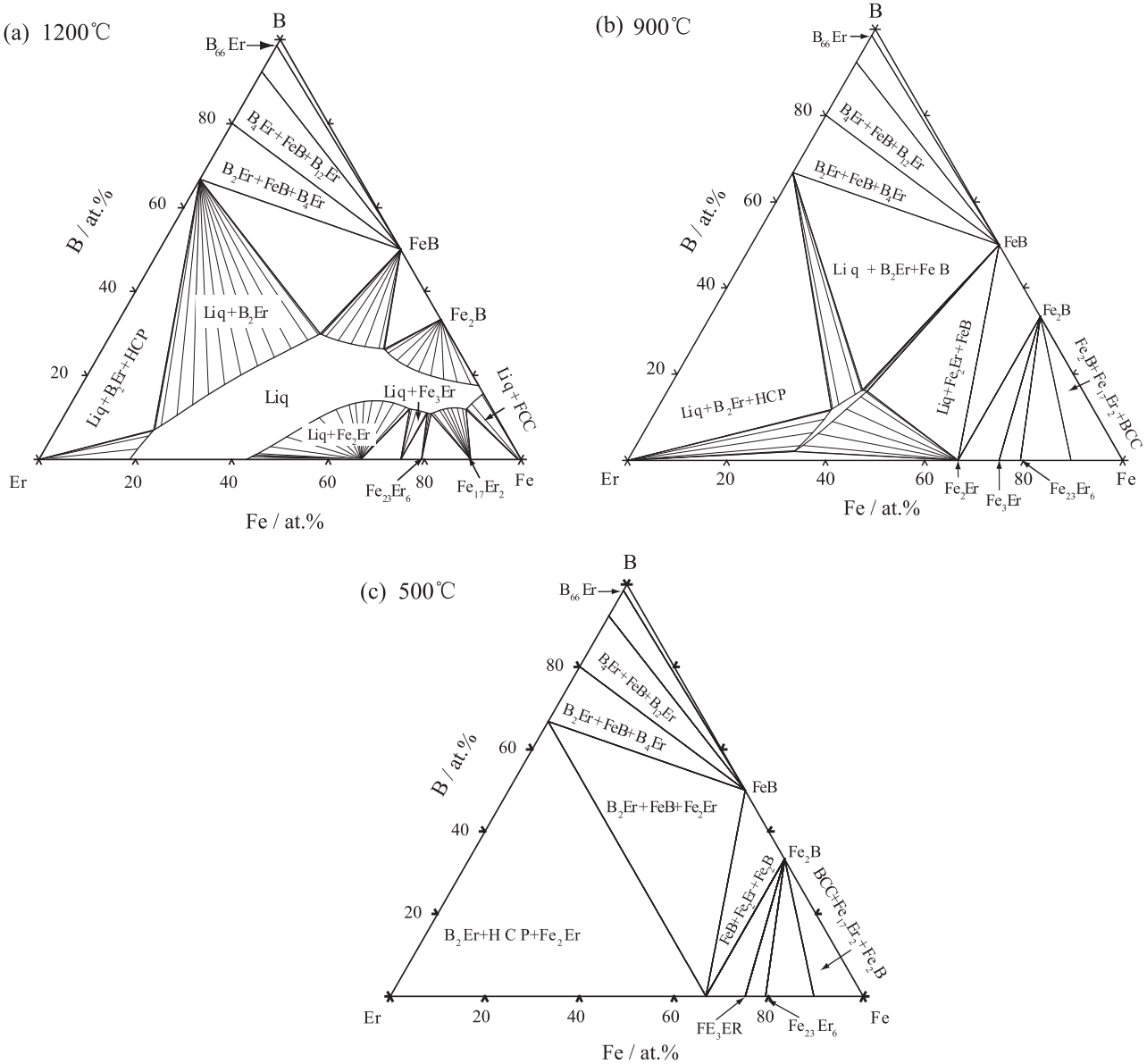


Fig. 8. Calculated isothermal section diagrams of the Fe–B–Er system at (a) 1200 °C, (b) 900 °C and (c) 500 °C.

surface gives much useful information for further determination of the phase equilibria by experiments.

5. Study of amorphous alloy in the Fe–B–Er system

One of the earliest and simplest methods for choosing amorphous alloy compositions has been to center alloys around deep eutectics [36,37]. From the calculated liquidus surface in the above section, it is actually easy to find out the eutectic point and fixed the position of possible composition of amorphous alloy. According to the liquidus surface, the eutectic points of E₁, E₂ and E₃ are selected for experiments.

The ingots of eutectic compositions in the Fe-rich region were prepared by arc melting with pure metals of 99.9 wt.% Fe, 99.9 wt.% Er and the Fe-17.49 wt.% B alloy in the Ti-gettered argon atmosphere. The ingots were remelted at least three times to make its composition homogeneous. The amorphous ribbons with thickness of 30 μm were prepared by a single-roller melt-spinning technique. The structure of ribbons was examined by X-ray diffraction (XRD) using Panalytical X'pert with Cu Kα radiation. XRD patterns of

ribbons are plotted in Fig. 10. It is seen that the XRD pattern of E₁ sample appears some sharp peaks in both sides, which indicates a structure of full crystallization. The XRD pattern of E₂ sample appears a weak peak only in the back side, which indicates a structure of partial amorphous. The E₃ sample, however, presents a broad diffraction hump in the XRD pattern of both sides, which confirms the full amorphous feature.

The distinct results demonstrate that the GFA of E₂ and E₃ samples is better than that of E₁ sample. The main reasons in the context of Fe–B–Er phase diagram can be summarized as follows: (1) the temperatures of eutectic reaction in E₂ (1107.9 °C) and E₃ (1107.8 °C) samples are lower than that of E₁ sample. Thus, the samples with lower melting point should have a better GFA [3]; (2) Wu et al. [38] argued that solid solution has a certain composition range, thus, the formation of solid solution phase by the diffusion of atoms during the melt cooling process is much easier compared with compounds with strict stoichiometric proportion. Consequently, when the solid solution phase precipitates as the primary phase, the alloy has a relatively weak GFA. From Table 6, the primary phases in E₁ sample include solution phase (γ Fe).

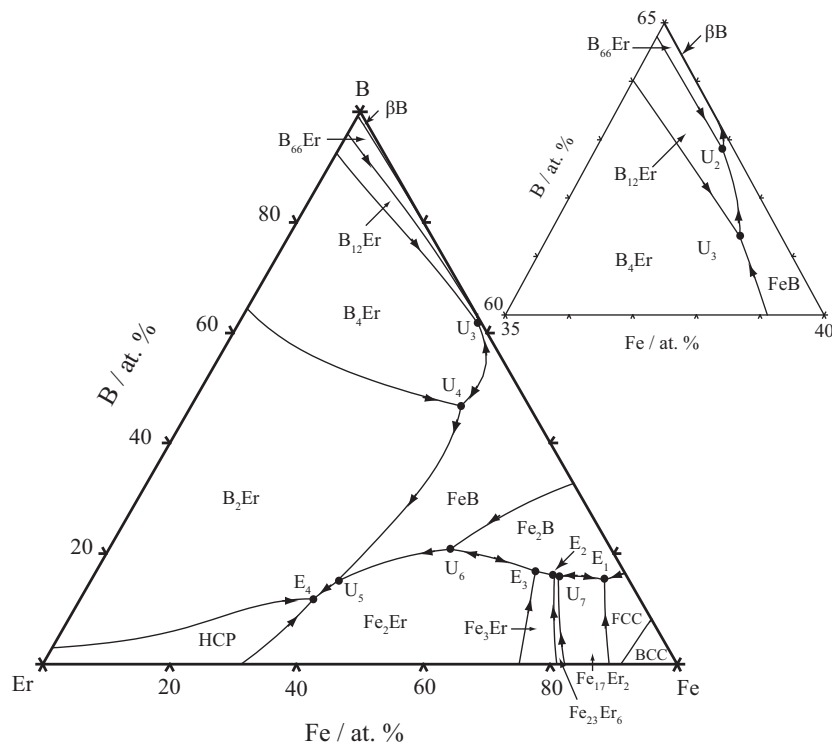


Fig. 9. The calculated liquidus surface of the Fe–B–Er system.

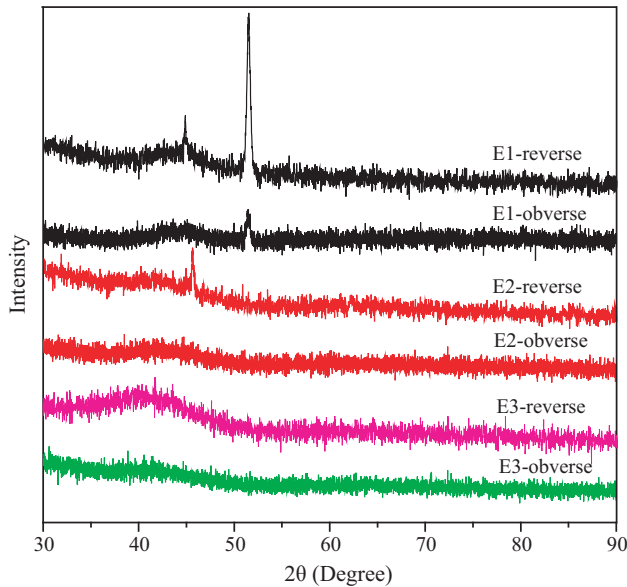


Fig. 10. X-ray diffraction pattern of the ribbons.

Compared with E₂ and E₃ samples which only contain compounds, E₁ sample has a stronger tendency to crystallization.

In a word, seeking for the eutectic points by thermodynamic calculation is an effective method to design the compositions of Fe-based amorphous alloys in the multicomponent system.

6. Conclusions

The phase diagrams in the Fe–Er and B–Er binary systems were thermodynamically assessed by considering the experimental data including phase equilibria and thermodynamic data. A consistent set of thermodynamic parameters has been optimized and most

of the experimental information can be satisfactorily reproduced on the basis of the optimized thermodynamic parameters. In addition, the liquidus surface of the Fe–B–Er ternary system has been calculated by means of CALPHAD and the investigation of GFA for the alloys in the Fe–B–Er liquidus surface proves the significance of calculated phase diagram in the composition design of Fe-based amorphous alloy.

Acknowledgements

This work was jointly supported by the National Natural Science Foundation of China (Nos. 51031003, 50425101), the Ministry of Science and Technology, PR China (2009DFA52170), the Ministry of Education, PR China (No. 707037).

References

- [1] A. Inoue, B. Shen, A. Takeuchi, Mater. Trans. 47 (2006) 1275–1285.
- [2] H. Matsumoto, A. Urata, Y. Yamada, A. Inoue, J. Alloy Compd. 509 (2011) S193–S196.
- [3] T.L. Wang, W.C. Wang, J.H. Li, B.X. Liu, J. Alloy Compd. 493 (2010) 154–157.
- [4] S.F. Guo, N. Li, C. Zhang, L. Liu, J. Alloy Compd. 504 (2010) S78–S81.
- [5] H. Jian, W. Luo, S. Tao, M. Yan, J. Alloy Compd. 505 (2010) 315–318.
- [6] M.G. Nabialek, M.J. Dośpiał, M. Szota, P. Pietrusiewicz, J. Jędrzyka, J. Alloy Compd. 509 (2011) 3382–3386.
- [7] Z.Z. Yuan, S.L. Bao, Y. Lu, D.P. Zhang, L. Yao, J. Alloy Compd. 459 (2008) 251–260.
- [8] D. Turnbull, Contemp. Phys. 10 (5) (1969) 473–488.
- [9] Ferenc, J. Erenc-Sedziak, T. Kowalczyk, M. Kulik, J. Alloy Compd. 495 (2010) 327–329.
- [10] H.B. Cao, Y. Pan, L. Ding, C. Zhang, J. Zhu, K.C. Hsieh, Y.A. Chang, Acta Mater. 56 (2008) 2032–2039.
- [11] D. Ma, H. Cao, Y.A. Chang, Intermetallics 15 (2007) 1122–1126.
- [12] H. Ma, L.L. Shi, J. Xu, Y. Li, E. Ma, Appl. Phys. Lett. 87 (2005) 181915.
- [13] Z.P. Lu, C.T. Liu, W.D. Porter, Appl. Phys. Lett. 83 (2003) 2581.
- [14] Z.P. Lu, C.T. Liu, J.R. Thompson, W.D. Porter, Phys. Rev. Lett. 92 (2004) 245503.
- [15] M. Iqbal, J.I. Akhter, H.F. Zhang, Z.Q. Hu, J. Non-Cryst. Solids 354 (2008) 3284.
- [16] W.H. Wang, Prog. Mater. Sci. 52 (2007) 540–596.
- [17] C.Y. Lin, H.Y. Tien, T.S. Chin, Appl. Phys. Lett. 86 (2005) 162501.
- [18] G.J. Zhou, Z.W. Liu, D.C. Zeng, Z.P. Jin, Physica B 405 (2010) 3590.
- [19] K.H.J. Buschow, A.S. Van der Goot, Phys. Status Solidi 35 (1969) 515–522.
- [20] A. Meyer, J. Less-Common Met. 18 (1969) 41–48 (in German).

- [21] V.E. Kolesnikov, V.F. Trekhova, E.M. Savitskii, Izv. Akad. Nauk SSSR, Neorg. Mater. 7 (3) (1971) 495–497 (in Russian).
- [22] H. Okamoto, in: H. Okamoto (Ed.), Phase Diagrams of Binary Iron Alloys, ASM International, Materials Park, OH, 1993, pp. 341–349.
- [23] K.H.J. Buschow, Rep. Prog. Phys. 40 (1977) 1179.
- [24] S. Norgren, F. Hodaj, P. Azay, C. Colinet, Metall. Mater. Trans. A 29 (1998) 1367.
- [25] R.W. Mar, N.D. Stout, J. Chem. Thermodyn. 6 (1974) 943–947.
- [26] E.G. Impearo, Ph.D. Thesis in Solid State Science, The Pennsylvania State University, University Park, PA, 1976.
- [27] K.E. Spear, Phase Diagrams: Materials Science and Technology, Academic Press, New York, 1976, pp. 91–159.
- [28] P.K. Liao, K.E. Spear, J. Phase Equilib. 17 (4) (1996) 326–329.
- [29] S.V. Meschel, O.J. Kleppa, J. Chim. Phys. 94 (1997) 928–938.
- [30] A.T. Dinsdale, SGTE Pure Elements (unary) Database, Version 4.4, 2001.
- [31] O. Redlich, A.T. Kister, Ind. Eng. Chem. 40 (1948) 345–348.
- [32] M. Hillert, M. Jarl, CALPHAD 2 (1978) 227–238.
- [33] B. Sundman, B. Jansson, J.O. Andersson, CALPHAD 9 (1985) 153–190.
- [34] H. Okamoto, in: H. Okamoto (Ed.), Phase Diagrams of Binary Iron Alloys, ASM International, Materials Park, OH, 1994, pp. xxxix–xliv.
- [35] B. Hallemans, P. Wollants, J.R. Roos, Z. Metallkd. 85 (10) (1994) 676–682.
- [36] M. Marcus, D. Turnbull, Mater. Sci. 23 (1976) 211.
- [37] J. Cheney, K. Vecchio, Mater. Sci. Eng. A 471 (1–2) (2007) 135–143.
- [38] Y. Wu, X.D. Hui, Z.P. Lu, Z.Y. Liu, L. Liang, G.L. Chen, J. Alloy Compd. 467 (2009) 187–190.
- [39] T.B. Massalski, H. Okamoto, P.R. Subramanian, L. Kacprzak, M.E. Kissner, Binary Alloy Phase Diagrams, vol. 2, 2nd ed., 1992, p. 1852.